`

Supporting Information Appendix

Synchronous volcanic eruptions and abrupt climate change ~17.7k years ago plausibly linked by stratospheric ozone depletion

Joseph R. McConnell, Andrea Burke, Nelia W. Dunbar, Peter Köhler, Jennie L. Thomas, Monica M. Arienzo, Nathan J. Chellman, Olivia J. Maselli, Michael Sigl, Jess F. Adkins, Daniel Baggenstos, John F. Burkhart, Edward J. Brook, Christo Buizert, Jihong Cole-Dai, T.J. Fudge, Gregor Knorr, Hans-F. Graf, Mackenzie M. Grieman, Nels Iverson, Kenneth C. McGwire, Robert Mulvaney, Guillaume Paris, Rachael H. Rhodes, Eric S. Saltzman, Jeffrey P. Severinghaus, Jørgen-Peder Steffensen, Kendrick C. Taylor, Gisela Winckler

Contents

1. **Continuous Ice Core Measurements (Figs. S1a-d, S2a-c)**
2. **Discrete Ice Core Measurements (Fig. S3)**
3. **Bromine and Bromide**
4. **Tephra Sampling and Geochemistry (Table S1)**
5. **Mt. Takahe Emission Estimates**
6. **Evidence for Reversible Bromine Deposition in Antarctic Snow (Fig. S4)**
7. **Snowpack Modeling (Figs. S5, S6)**
8. **Comparisons to Modern Ozone Depletion**
9. **AOGCM Simulations (Fig. S7)**
10. **Fig. S8**

`

Continuous Ice Core Measurements

Longitudinal WD samples from ~1300 m to ~2710 m depth were analyzed for a broad range of elements and chemical species using a state-of-the-art continuous ice core analytical system (SI Appendix, Fig. S8), in addition to replicate WD samples from 2419.3 m to 2435.2 m and all samples of the Byrd core between 1242.06 to 1303.39 m depth available from the University of Copenhagen archive. The 3404 m long WD ice core (79.481^{o}S, 112.112^{o}W, 1766 m elevation) was collected from a cold (mean annual temperature -31^{o} C), high snowfall (196 kg m^{-2} y^{-1}) West Antarctic site (3). Because the core also was measured with high-resolution analytical techniques, WD provides the highest temporal resolution Antarctic climate record available for the last glacial to interglacial transition. The WD record exceeds the temporal resolution of the deep Greenland cores – GISP2, GRIP, NGRIP, NEEM – and includes a much broader range of aerosol-linked elemental and chemical tracers. The Byrd core was collected in 1968 from a site (80.02^{o}S, 119.52^{o}W) located 159 km from WD and ~200 m lower in elevation (4). Similar continuous analyses of ice samples from Taylor Glacier in the Antarctic Dry Valleys (5) provided an additional record of the 17.7ka Mt. Takahe event (Fig. 3).

Analyses were conducted on longitudinal samples (~100 mm by ~33 mm by ~33 mm) using the Desert Research Institute's well-established, continuous-flow analysis with trace elements and black carbon analytical system (6-12), recently expanded to include continuous measurements of mineral acidity (13) and CH_4 (14). The analytical system included two Element2 (Thermo Scientific) high-resolution inductively coupled plasma mass spectrometers (HR-ICP-MS) operating in parallel for measurement of a broad range of ~35 elements, an SP2 (Droplet Measurement Technologies) inter-cavity-laser-based instrument for black carbon (BC) measurements, and a number of fluorimeters and spectrophotometers for measurement of ammonium, nitrate, hydrogen peroxide, and other chemical species (SI Appendix, Fig. S8). All measurements were exactly co-registered in depth. While effective measurement resolution differed between sample streams and instruments, resolution typically was less than 10 mm for aerosol-related elements and chemical species.

Comparisons of replicate measurements from within the WD core (SI Appendix, Fig. S1) and between the WD and Byrd ice cores (SI Appendix, Fig. S2) indicate that results were highly repeatable for nearly all elements, despite the extremely low concentration levels (as low as 20 fg g^{-1}) for elements such as the low-boiling-point heavy metals (bismuth, cadmium, and thallium) and REE (lanthanum, cerium, and europium), and despite the distance between the WD and Byrd coring sites. Note the near-perfect replication of the observed bromine depletion during the 17.7ka anomaly. Under recovery of more recalcitrant elements such as Al and Fe contained in larger insoluble dust particles is implicit in continuous methods (11, 15) but does not impact measurements of heavy metals or other elements associated with gaseous volcanic emissions that generally coat the outside of insoluble particles because of the addition of ultra-pure nitric acid to the sample flow stream immediately after the melter head.

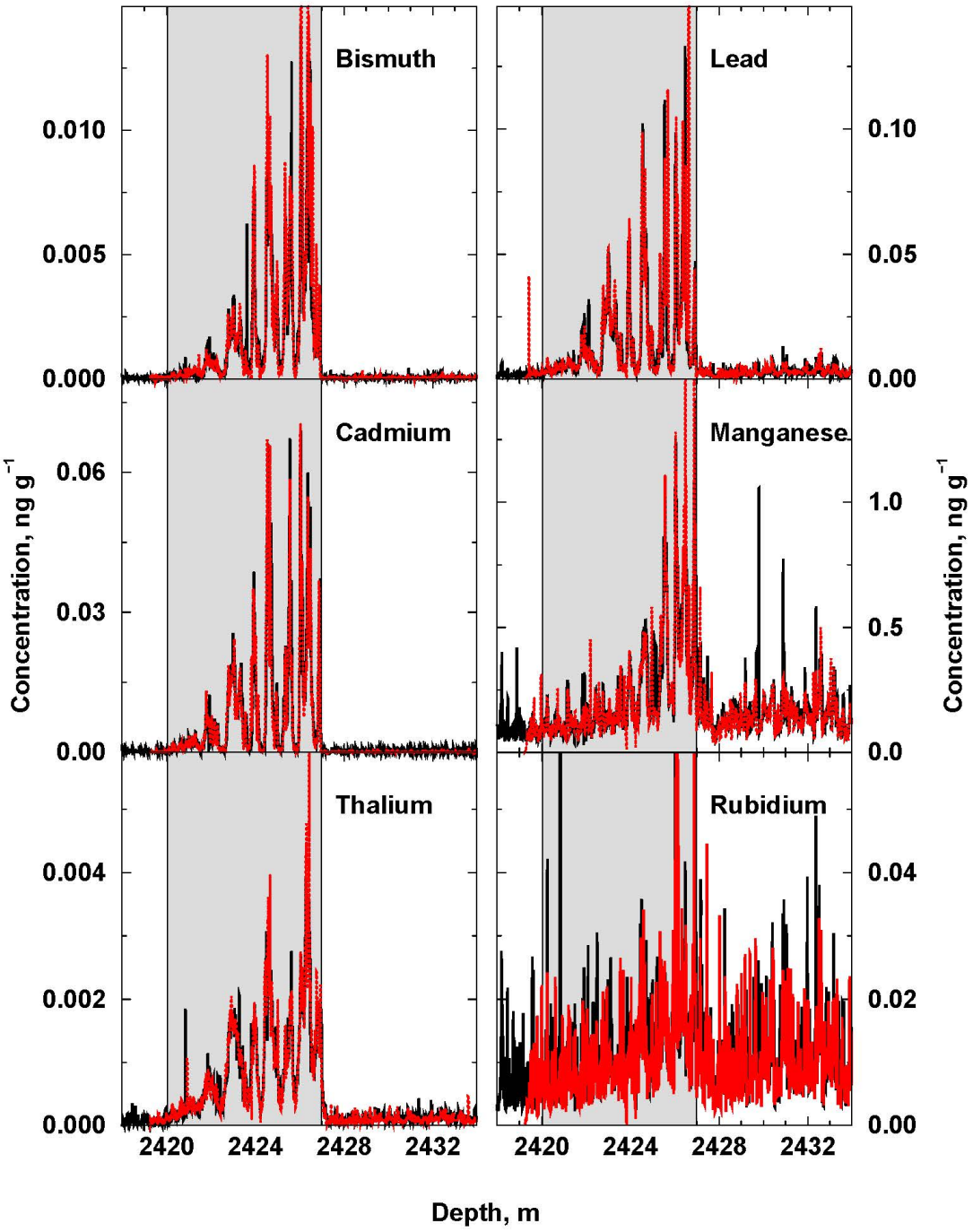

Fig. S1a-d Continuous, high-resolution measurements of selected elements and insoluble particle counts (PC) in the WAIS Divide (WD) ice core. The shaded box identifies the period of the 17.7ka anomaly in WD. Size-specific dust concentrations were calculated from insoluble particle counts. Comparison of original (black) and replicate (red) measurements on a second set of longitudinal samples shows that the measurements are highly repeatable despite the extremely low concentrations and high variability of many elements (Dataset S1).

`

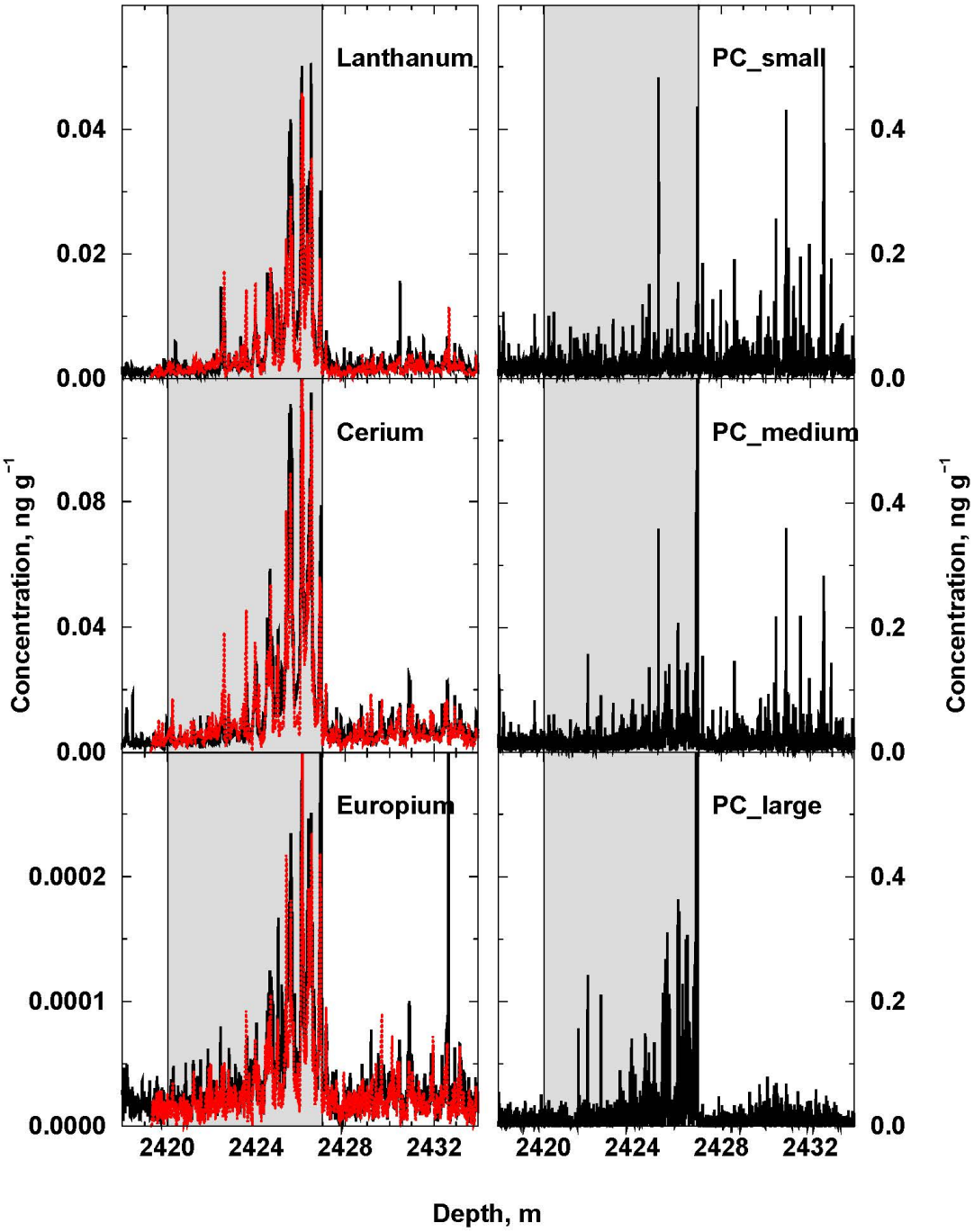
Lanthanum
Cerium
Europium
PC_small
PC_medium
PC_large
Concentration, ng g^{-1}
Concentration, ng g^{-1}
0.04
0.02
0.00
0.08
0.04
0.00
0.0002
0.0001
0.0000
0.4
0.2
0.0
0.4
0.2
0.0
0.4
0.2
0.0
2420
2424
2428
2432
2420
2424
2428
2432
Depth, m

Fig. S1b

`

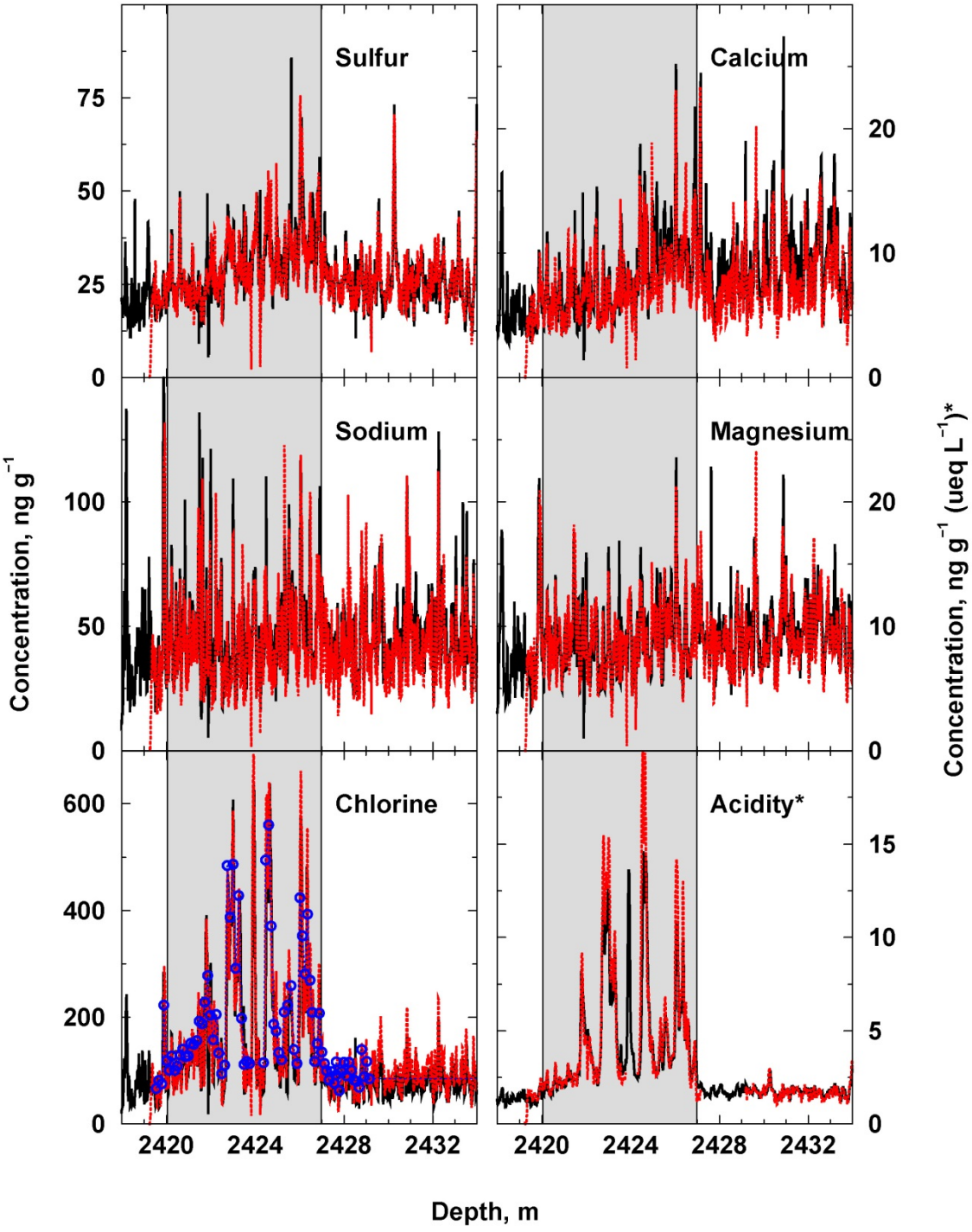
Sulfur
Calcium
Sodium
Magnesium
Chlorine
Acidity*
Concentration, ng g^{-1}
Concentration, ng g^{-1} (ueq L^{-1})*
Depth, m
0
25
50
75
100
200
400
600
5
10
15
20
2420
2424
2428
2432

Fig. S1c

`

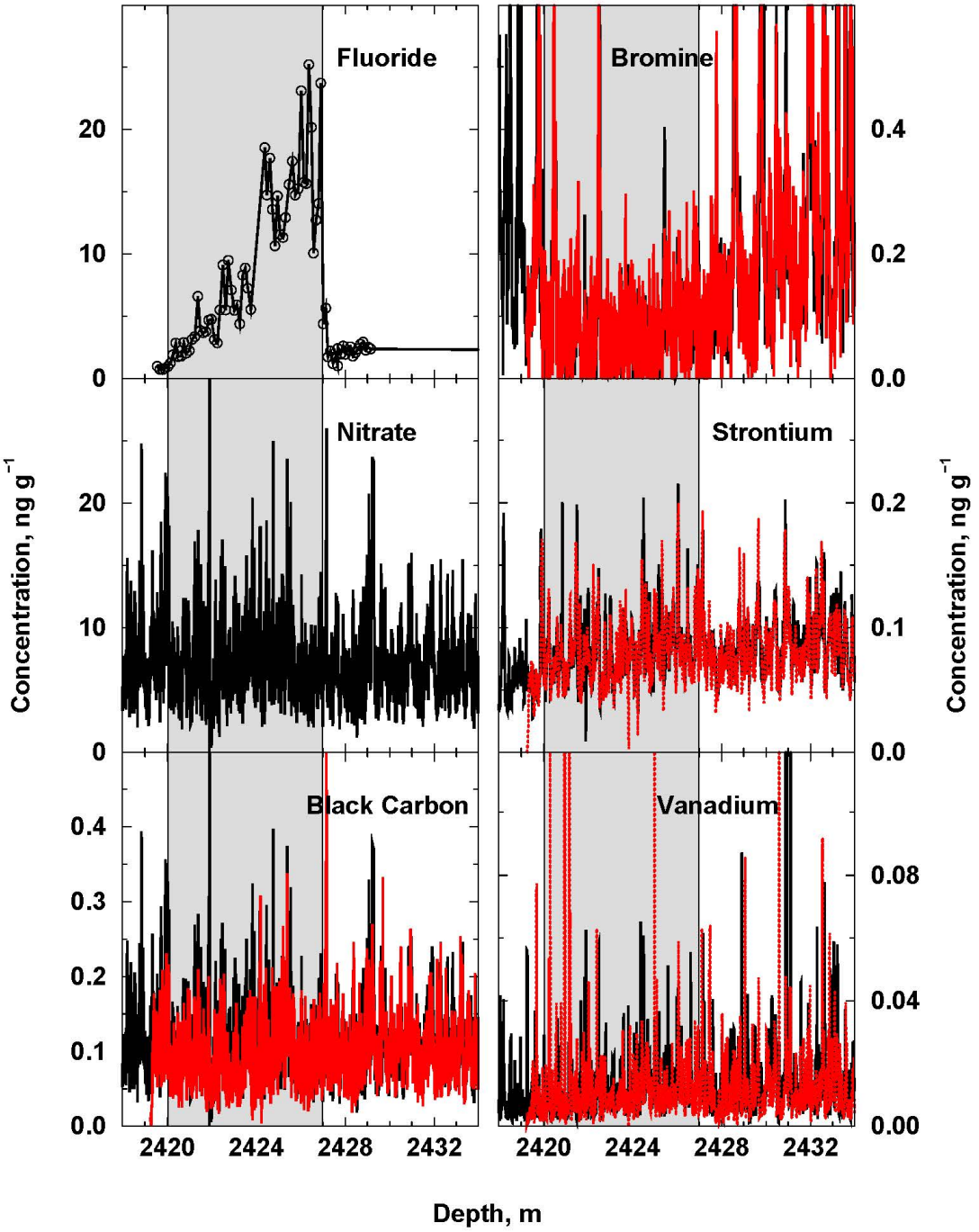
Fluoride
Bromine
Nitrate
Strontium
Black Carbon
Vanadium
Concentration, ng g^{-1}
Concentration, ng g^{-1}
Depth, m
2420
2424
2428
2432

Fig. S1d

`

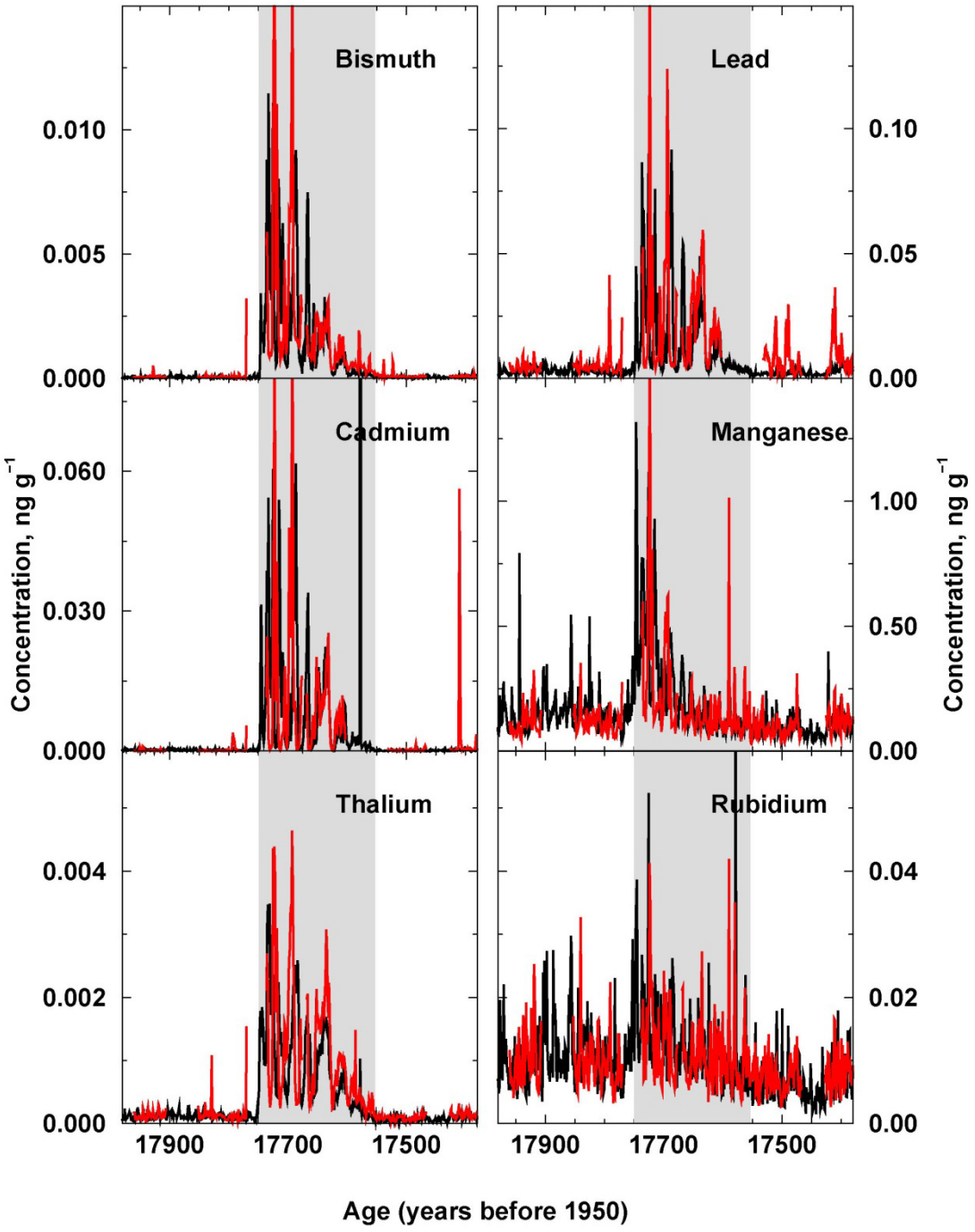

Fig. S2a-c Comparison of continuous, high-resolution measurements of selected elements in the Byrd and WD ice cores. WD measurements (black) are shown on the WD2014 timescale. The shaded box identifies the period of the 17.7ka anomaly in WD. Byrd (4) measurements (red) were made on all available samples from the University of Copenhagen archive and synchronized to WD using 20 volcanic markers between 1241 and 1295 m depth in the Byrd core. Note the very close agreement in the WD and Byrd records for all parameters despite the nearly 50-year storage time, limited contiguity of available samples from Byrd, and 159 km distance between the sites (Dataset S1).

`

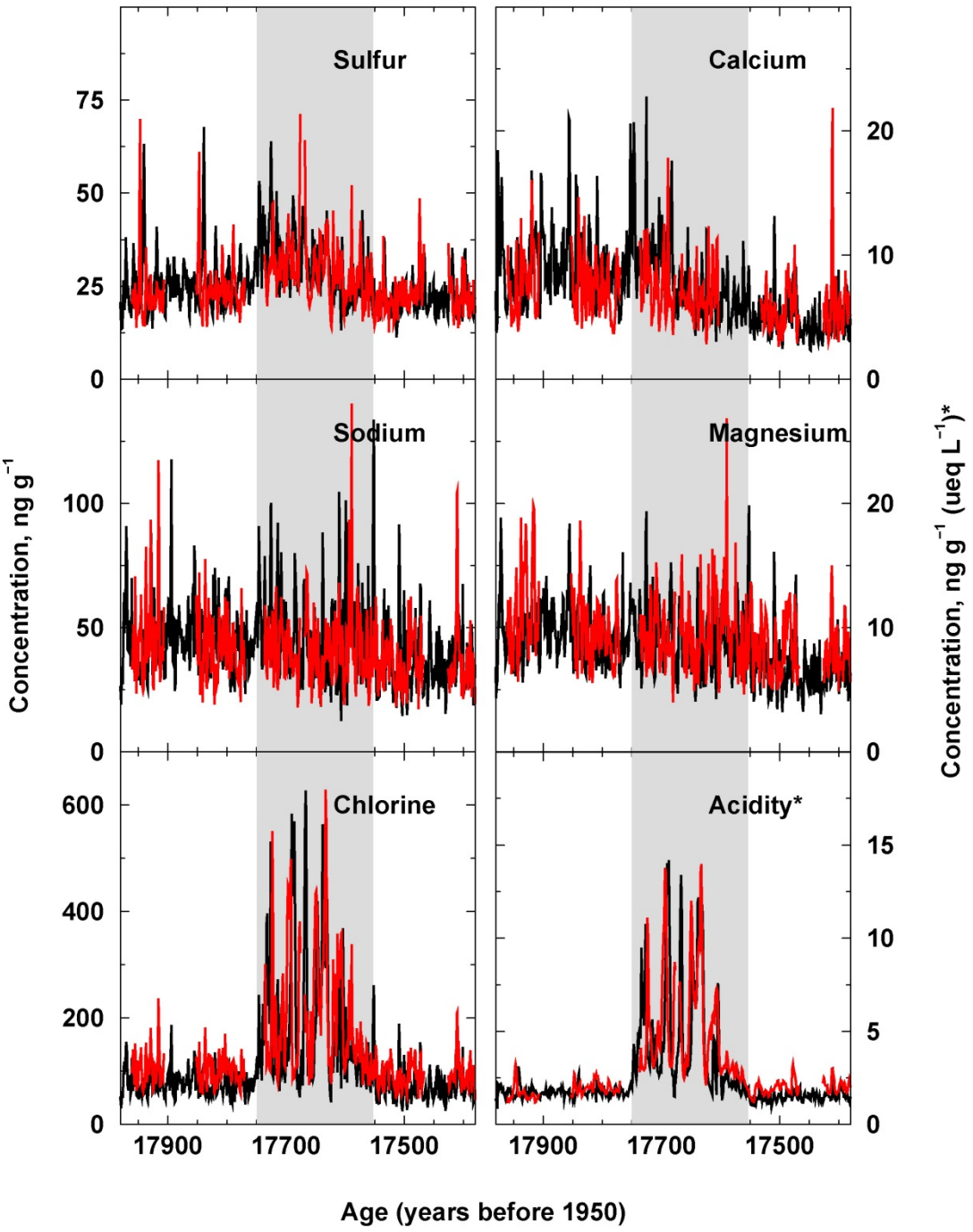
Sulfur
Calcium
Sodium
Magnesium
Chlorine
Acidity*
Concentration, ng g^{-1}
Concentration, ng g^{-1} (ueq L^{-1})*
Age (years before 1950)
17900
17700
17500

Fig. S2b

`

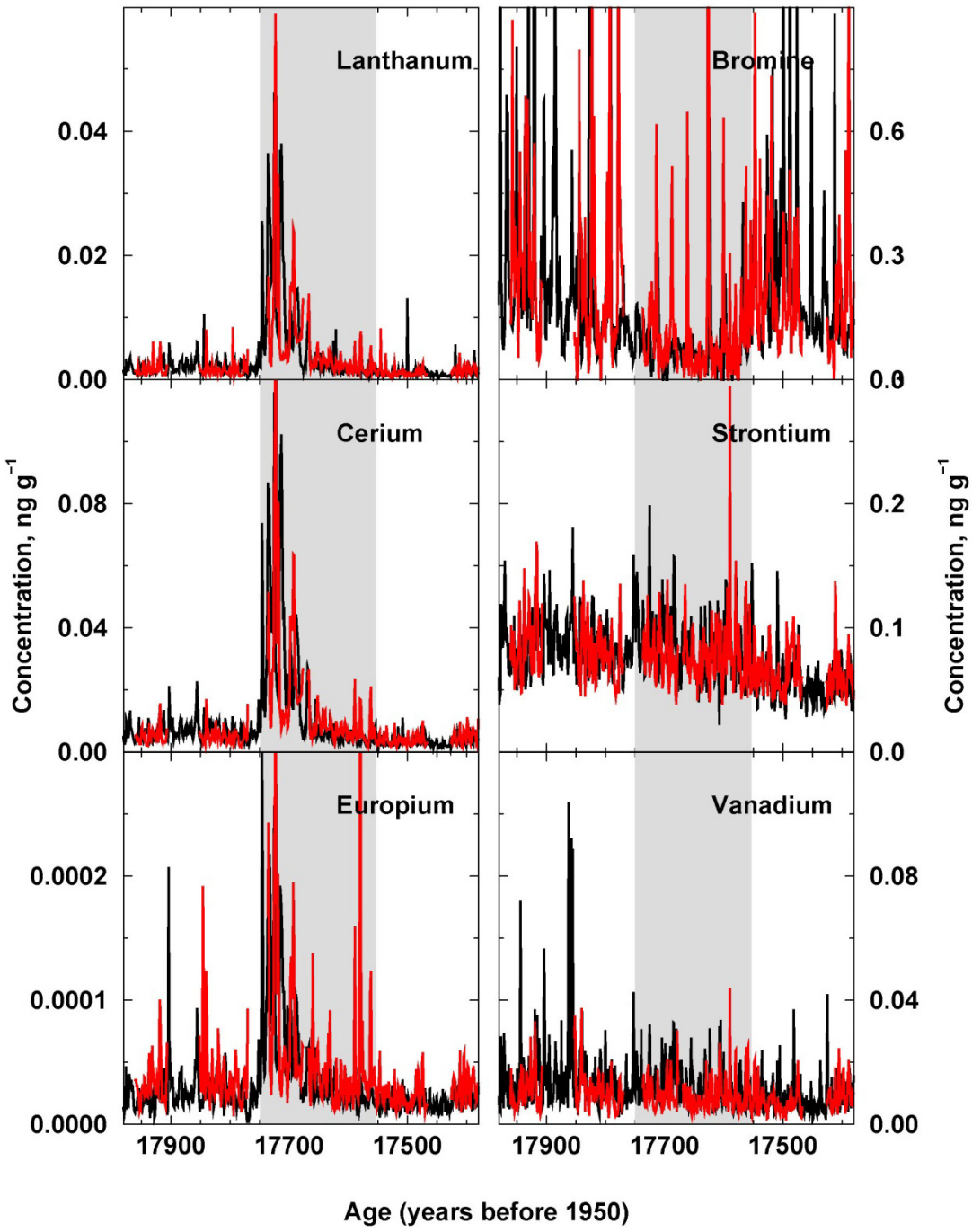
Lanthanum
Bromine
Cerium
Strontium
Europium
Vanadium
0.04
0.02
0.00
0.6
0.3
0.0
0.08
0.04
0.00
0.2
0.1
0.0
0.0002
0.0001
0.0000
0.08
0.04
0.00
17900
17700
17500
Concentration, ng g-1
Age (years before 1950)

Fig. S2c

`

Discrete Ice Core Measurements

Fluoride, bromide, and some other compounds cannot be measured with the on-line system so discrete samples were captured using a fraction collector during continuous analysis of the primary, replicate, and Byrd samples. Discrete samples were analyzed for fluoride, chloride, sulfate, and methane sulfonic acid (MSA) using ion chromatography (IC), as well as bromide and MSA using anion chromatography with detection by electrospray ionization and negative ion tandem mass spectrometry. Comparisons between the continuous ICP-MS measurements of chlorine and the discrete IC measurements of chloride show that the results are similar (SI Appendix, Fig. S3) and a pronounced depletion at 17.7ka was observed in both discrete bromide and continuous (16) bromine concentrations (SI Appendix – Bromine and Bromide).

Sulfur isotopes were measured on selected discrete samples using multi-collector ICP-MS (17).

Approximately 3 kg discrete meltwater samples were collected from the outer ring of the melter head for He concentration and isotope measurements above, within, and below the 17.7ka event. Average ^{3}He concentrations were 4.4e-17 (±2.5e-17) cm^3 g^{-1} and 3.7e-17 (±2.5e-17) cm^3 g^{-1} in the five background and four 17.7ka event samples, respectively. Similarly, the $^{3}He/^{4}He$ ratios were 6.8e-5 (±1.7e-5) in the background samples and 7.3e-5 (±1.9e-5) in the event samples.

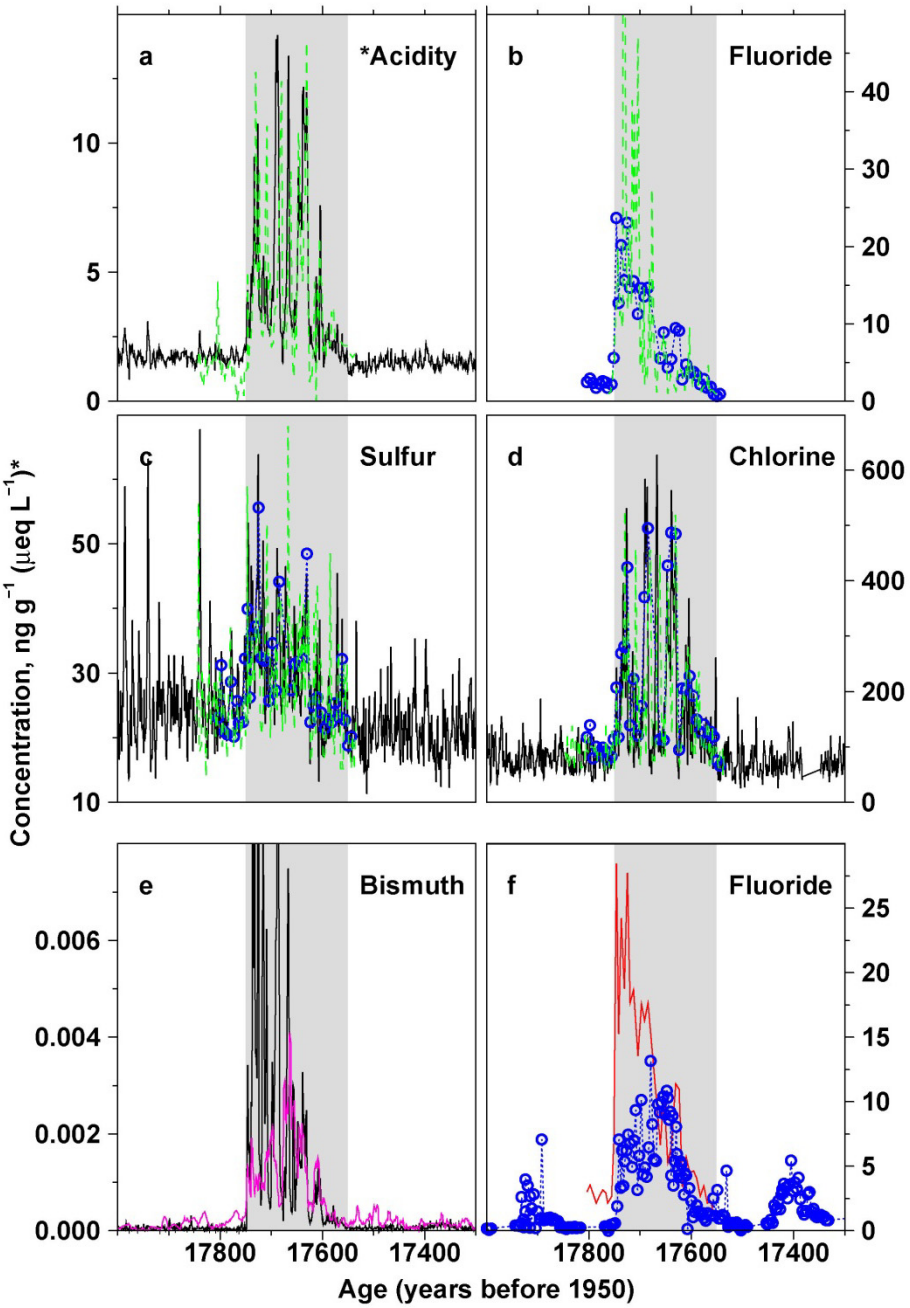

Fig. S3 Measurements showing the spatial extent of the ~17.7ka glaciochemical anomaly. (a-d): Measurements of acidity, sulfur (sulfate), and the halogens chlorine (chloride) and fluoride in the WD ice core and original (4) measurements from the Byrd ice core. Byrd measurements are shown in green (dashed line). Original continuous measurements on the WD core (Dataset S1) are shown in black with ion chromatography measurements on WD discrete samples (Dataset S1) shown in blue (circles). All the Byrd measurements are shown on the original timescale but shifted in age by 230 years to align with WD. (**e):** Bismuth measured in the WD and Taylor Glacier (magenta) cores (Dataset S1). (**f):** Fluoride measured in the WD and EDC cores (Dataset S1). The shaded boxes in **a-f** identify the period of the 17.7ka anomaly in WD.

`

Bromine and Bromide

Although often close to detection limits when measured using ion chromatography, bromide (Br^-) rarely has been measured in ice cores previously. It has been studied extensively, however, in near-surface polar snow because bromine plays an important role in snowpack photochemistry (18-20). Here we measured both total bromine (Br_{total}) and Br^- concentrations in the WD core. Good agreement was found between Br_{total} and Br^- concentrations in samples corresponding to the 17.7ka Mt. Takahe event, with both showing nearly complete depletion during the volcanic event (Fig. 1).

Br_{total} was measured continuously in the WD and Byrd cores using methods described in Maselli et al. (16). Br^- was measured in discrete samples from WD obtained using a fraction collector from the DRI continuous melter (SI Appendix, Fig. S8). Note that the discrete samples were collected from a different part of the ice core cross section than the continuous sample melt stream. The discrete samples were analyzed using anion chromatography with detection by electrospray ionization and negative ion tandem mass spectrometry (ESI/MS/MS; Thermofinnigan Quantum). The chromatography used a 1 ml injection loop, and a 2 x 150 mm AS 18 fast anion column with 0.04 M KOH eluent at a flow rate of 200 ul/min (Dionex ICS-2100 ion chromatograph). The eluent stream was mixed with 0.07 µl/min of methanol prior to entering the electrospray ion source. Bromide was detected as $^{79}Br^-$ and quantified using gravimetrically calibrated aqueous NaBr standards. The bromide signal at mass 81 also was monitored to verify the identity of the bromide peak using the bromine 79/81 isotopic ratio.

`

Tephra Sampling and Geochemistry

Continuous measurements showing high concentrations of REE, manganese, and other elements (SI Appendix, Fig. S1) found in tephra, as well as modest but clear increases in insoluble particles in the 2.5 to 10 μm range during the early stages of the 17.7ka event, indicated that tephra particles were present. During replicate continuous analyses of the main WD core, 10 μm, stainless-steel, in-line filters were added to the two lines coming from the middle ring of the melter head (SI Appendix, Fig. S8) to capture volcanic tephra particles present in the meltwater stream. Sets of filters were collected for a background section of WD ice with no chemical evidence of volcanic fallout, as well as two sets of filters representing the early and later stages during the extended volcanic period. All pairs of filters subsequently were back-flushed vigorously with ultra-pure water to release any captured particles; the back-flushed solution samples were filtered and then prepared for electron microprobe analysis following standard procedures for volcanic tephra analyses (21). Following targeted replicate coring efforts to recover two additional complete cores from this depth interval, tephra samples also were collected from the first three of nine total pulses of volcanic fallout in the overall ~192-year event. Small concentrations of silicate particles were detected for the depth interval corresponding to the early stages of the 17.7ka event (2430–2426 m). No glass shards were found in the background sample or in the sample corresponding to the later stages of the 17.7ka event, consistent with the continuous insoluble particle measurements (SI Appendix, Fig. S1). Most of the particles identified in the sample were fine (~10 μm), and some had cuspate shapes suggestive of volcanic origin. The geochemistry of individual glass shards was analyzed using a Cameca SX-100 electron microprobe [see methods in (21, 22)]. Results are summarized in Table S1.

Mt. Takahe, a heavily glaciated West Antarctic volcano, is characterized by an unusual, 8 km wide summit caldera (23). This feature is unique among West Antarctic stratovolcanoes and is unusual even in a global context. The flat-topped nature of Mt. Takahe initially was thought to be a result of completely sub-glacial volcanism, resulting in a characteristic “table mountain” form, but subsequent fieldwork revealed significant sub-aerial volcanism on the upper parts of the volcano, thereby ruling out sub-glacial origin (24). The flat-topped shape of Mt. Takahe remains enigmatic. Note that the halogen-rich and tephra-poor characteristics of the event fallout are similar to modern emissions from Mt. Erebus (25) and Mt. Etna. Because of the degree of glaciation, the chronological record of explosive volcanism at Mt. Takahe is incomplete. Explosive events have been dated at 8.2±5.4ka, 93.3±7.8ka, and 102±7.4ka (26). Eruptive events, sampled as lavas, also occurred at Mt. Takahe at 7±6, 29±12, 34±8, 39±14, 45±8, 50±15, and 104±28ka (27) so eruptive activity in the age range of 17.7ka is consistent with the volcano’s overall eruptive patterns.

Table S1. Major element composition of tephra shards from the main and replicate WD ice cores, with representative compositions for West Antarctic volcanoes Mt. Takahe and Mt. Berlin.

Depth Range m	n	P_2O_5	SiO_2	SO_2	TiO_2	Al_2O_3	MgO	CaO	MnO	FeO	Na_2O	K_2O
2430.0-2426.0 (WD main core)	4	0.29 (±0.02)	61.70 (±0.76)	0.25 (±0.05)	0.87 (±0.12)	14.98 (±0.31)	0.50 (±0.00)	2.10 (±0.09)	0.32 (±0.08)	8.89 (±0.18)	5.02 (±1.18)	4.66 (±0.22)
2426.05-2426.60 (Replicate core)	40	0.22 (±0.05)	60.54 (±0.74)	0.12 (±0.05)	0.87 (±0.08)	15.29 (±0.50)	0.54 (±0.11)	2.14 (±0.14)	0.32 (±0.06)	8.41 (±0.56)	6.31 (±0.61)	4.75 (±0.14)
2425.50-2426.30 (Replicate core)	27	0.25 (±0.05)	60.20 (±0.96)	0.13 (±0.06)	0.90 (±0.08)	15.24 (±0.58)	0.52 (±0.11)	2.11 (±0.35)	0.33 (±0.06)	8.78 (±0.61)	6.06 (±0.63)	4.79 (±0.37)
2425.75-2425.25 (Replicate core)	8	0.22 (±0.05)	61.11 (±0.69)	0.13 (±0.04)	0.83 (±0.12)	15.12 (±0.20)	0.55 (±0.12)	1.98 (±0.28)	0.32 (±0.04)	8.36 (±0.40)	6.17 (±0.52)	4.66 (±0.25)
Mt. Takahe		0.16	61.82	0.09	0.80	15.30	0.34	1.59	0.31	8.29	5.90	5.17
Mt. Berlin		0.04	62.57	0.08	0.52	13.88	0.00	1.03	0.26	8.84	7.69	4.69

Notes:

Geochemical quantities are in weight %. Analyses are normalized to 100 weight %. n equals number of analyses. Analytical precision based on replicate analyses of standard reference materials of similar composition to the unknowns (VG-568; KN-18; KE-12) are as follows (all in weight %): P_2O_5±0.02, SiO_2±0.47, SO_2±0.01, TiO_2±0.03, Al_2O_3±0.12, MgO±0.07, CaO±0.02, MnO±0.06, FeO±0.06, Na_2O±0.55, K_2O±0.27. Peak count times of 20 seconds were used for all elements with the exception of Na (40 seconds) and S (40 seconds). Primary calibration standards are: P_2O_5 and CaO Beeson apatite; SiO_2, K_2O, Al_2O_3 orth-1; TiO_2 rutile, MgO diopside, MnO MnO, FeO magnetite; Na_2O Amelia albite; SO_2 barite. Beam sizes used for analysis ranged between 10 and 15 μm, depending on the size of grain available. Replicate cores were sampled over depth ranges that contained individual volcanic pulses (Figs. 2, S1).

`

Mt. Takahe Emission Estimates

We estimated peak and average chlorine emissions during the ~192-year Mt. Takahe event based on the chlorine fallout measured in the WD, Byrd, and Taylor Glacier ice cores. Peak and average excess chlorine (observed fluxes minus background levels) at WD and Byrd (nearly identical at both sites) were ~74 and ~13 mg m^{-2} y^{-1}, respectively. At Taylor Glacier, peak and average fluxes were ~5.6 and ~1.5 mg m^{-2} y^{-1}, respectively. The WD, Byrd, and Taylor Glacier ice core sites are located approximately 350, 450, and 2000 km from Mt. Takahe, respectively. Assuming a radially symmetric, exponential drop off in fluxes away from the volcano results in peak chlorine emissions of ~400 Gg y^{-1}, with average emissions during the ~192-year event of 100 Gg y^{-1}. We emphasize that these only are order of magnitude estimates because so few measurements of the fallout are available. These levels are ~10 and ~40 times higher than modern emissions reported for nearby Mt. Erebus (28) and ~0.5 to ~2.5 times those reported for Mt. Etna (25). Mt. Etna currently is the largest point source in the world.

Reactive bromine is far more efficient than chlorine at destroying ozone in the stratosphere (29); but because bromine is reversibly deposited in the snowpack (SI Appendix – Snowpack Modeling), we were unable to use ice core measurements of fallout to estimate bromine emissions from the 17.7ka Mt. Takahe event. Assuming bromine-to-chlorine ratios as in modern emissions from Mt. Erebus (28), however, reactive bromine from Mt. Takahe likely also contributed to stratospheric ozone depletion.

`

Evidence for Reversible Bromine Deposition in Antarctic Snow

Evidence for reversible deposition of bromine and significant depletion can be found in modern Antarctic snowpacks. Sodium and bromine in Antarctic ice and snow derive primarily from ocean sources, but sodium is irreversibly deposited. Long-term average depositional fluxes for bromine and sodium measured in an array of 11 widely spaced ice cores from East and West Antarctica (7) are plotted against snowfall rate (SI Appendix, Fig. S4). This ice core array covers a broad range of snowfall rates ranging from 27 kg m^{-2} y^{-1} at NUS7-2 to 402 kg m^{-2} y^{-1} at DIV, and the chemical records span recent centuries to millennia. All of the core sites can be considered inland since all are located at least 200 km from the coast, so the snow chemistry is not heavily influenced by local marine sources.

SI Appendix, Fig. S4 shows depositional fluxes of bromine and sodium that were strongly dependent on snowfall rates. Using a simple linear model fit to the observed sodium flux versus snowfall (slope = 22.9 [±2.6]; intercept = -82 [±520]; R^2=0.945; $p < 0.0001$) shows that deposition was almost entirely through wet processes since the dry deposition term (intercept) is negligible when compared to the magnitude of the sodium concentrations. While bromine deposition also is well represented by this simple model (slope = 0.533 [±0.009]; intercept = -17.3 [±1.9]; R^2=0.999; $p < 0.0001$), the dry deposition term (intercept) is large relative to the wet deposition term (slope) and negative, indicating substantial release of bromine from the snowpack back to the atmosphere after deposition. That is, in modern snowpacks located both at high elevation, low-snowfall East Antarctic sites and lower elevation, high-snowfall West Antarctic sites, bromine was reversibly deposited with the initial flux to the surface linked to wet deposition processes. Concentrations preserved in the snow and ice were controlled almost entirely by the snowfall rate. Perhaps surprisingly, the re-emission rate does not appear to be related to the snow concentration as indicated by the very close fit (R^2=0.999) between the linear model and observations. For the mean snowfall rate in the array of 150 kg m^{-2} y^{-1}, >>99% of the sodium flux was through wet deposition based on the linear model, with no re-emission. For bromine, conversely, wet deposition was ~80 µg m^{-2} y^{-1}, but ~17 µg m^{-2} y^{-1} or about 22% was re-emitted into the atmosphere before the snow was buried, and the remaining bromine was preserved in the firn and ice. At sites with snowfall rates less than ~35 kg m^{-2} y^{-1}, nearly all bromine was re-emitted to the atmosphere prior to burial.

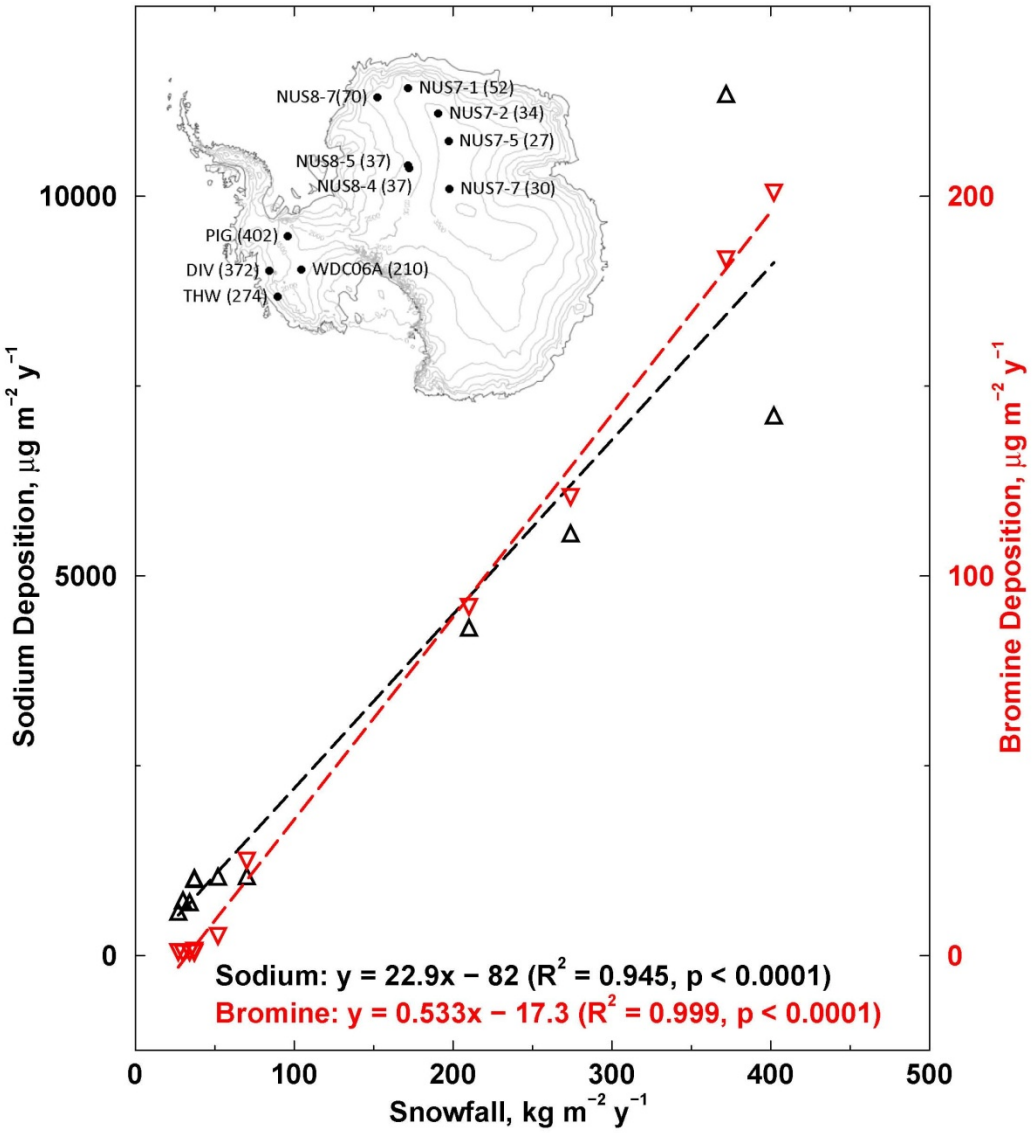

Fig. S4 Measurements of modern net deposition of bromine in an array of 11 Antarctic ice cores show the impact of reversible deposition. A linear model (dashed) fit to the average net deposition of sodium (black) and bromine (red) during recent centuries to millennia versus snowfall shows that while wet deposition accounts for nearly all of the flux of both elements (R^2 of 0.945 and 0.999 for sodium and bromine, respectively), bromine is reversibly deposited with a substantial portion (17.3±1.9 μg m^{-2} y^{-1}) re-emitted into the atmosphere prior to burial. Sodium is irreversibly deposited as shown by the small intercept compared to the measured concentrations. Inset shows the names and locations of the ice cores. Mean snowfall rates (kg m^{-2} y^{-1}) at each site are shown in parentheses.

`

Snowpack Modeling

The near-surface snowpack acts as a photochemical reactor (20, 30, 31), with a number of chemical species including reactive bromine and nitrate cycling between the air and snow. The result is substantial depletion in the snowpack if release into the atmosphere occurs more quickly than deposition followed by burial of the surface snow. The rate of release (loss) from the surface snow in part is determined by the duration and intensity of exposure of the snow to incoming UV radiation. Exposure duration is determined by the snow accumulation or burial rate since sunlight penetration below ~0.3 m (e-folding depth) in the snowpack is minimal (20). A large increase in UV radiation because of a decrease in the total ozone column will significantly increase exposure intensity during a fixed period of time, compared to the situation without a decrease in stratospheric ozone. Another possible factor determining bromine levels in surface snow may be acidity because the reactions that convert bromide into Br_2 that is subsequently released into the atmosphere are acid catalyzed (32).

The 17.7ka event in the WD and Byrd ice core record is characterized by sharp and sustained declines in bromine concentrations that occur with no detectable change in nitrate concentrations (Figs. 1) (SI Appendix, S1, S2). No anomalous increases in bromine concentration occurred at the start or end of the depletion, ruling out acidity-gradient-driven or other migration of bromine away from the 17.7ka anomaly, as has been reported for some ions (33). No change in snow accumulation was observed during the anomaly, indicating that there were no changes in exposure duration and pointing to increases in UV exposure intensity and possibly acidity increases as the likely cause of bromine loss during these events.

To evaluate the contribution of two factors on bromine and nitrate loss – (1) an increase in incoming UV radiation due to a reduction in stratospheric ozone, and (2) an increase in surface snowpack acidity – we used the 1-D coupled model of snow-atmosphere photochemistry MISTRA-SNOW. SI Appendix, Fig. S5 shows changes in bromine and nitrate concentrations in surface snow above an idealized 2 m snow column during a 72-hour model simulation. Initial concentrations at the surface are similar to those found today in the snow at WD, and concentrations decline exponentially from the surface.

For the control simulation, we used a typical modern total atmospheric ozone column burden of 300 Dobson Units (DU) with bulk acidity concentrations similar to those measured in the WD ice core. After 72 hours, average bromine concentrations in the surface-snow layer (0.01 m) and upper 1.0 m declined by ~7.8% and ~5.7%, respectively (SI Appendix, Fig. S5). Similarly, nitrate concentrations declined by ~3.3% in the surface snow and ~2.4% in the upper 1.0 m.

To evaluate sensitivity to atmospheric ozone changes, we repeated the control simulation but with total column ozone burdens varying from 50 to 250 DU (SI Appendix, Fig. S5). Re-emission of bromine increased with decreasing ozone burden, with approximately two-fold and three-fold increases in bromine loss for 50 DU compared with 300 DU for the surface-snow layer and upper 1.0 m of the snowpack, respectively. Nitrate losses also were sensitive to decreasing ozone burden but not nearly as sensitive as bromine.

`

Bromine and nitrate loss from the near-surface snowpack also may be sensitive to acidity concentrations through pH-dependent changes in reaction rates. To evaluate the sensitivity to acidity, we repeated the simulations but with two times the initial bulk H^+ concentrations and found substantially greater loss of bromine from both the surface snow and snowpack for all levels of total column ozone. Acid concentrations had little impact on nitrate loss in the model simulations. Taken together, the snowpack photochemistry model simulations suggest that bromine loss from the snow is more rapid than nitrate and that it is more sensitive to changes in total ozone column burden than acidity. In addition, simulations indicate that increasing the acidity of the snowpack enhances bromine loss for all ozone burdens but has little impact on nitrate loss. Thus, the lack of significant change in nitrate concentration observed during the 17.7ka event is consistent with ozone-hole-related changes in UV radiation.

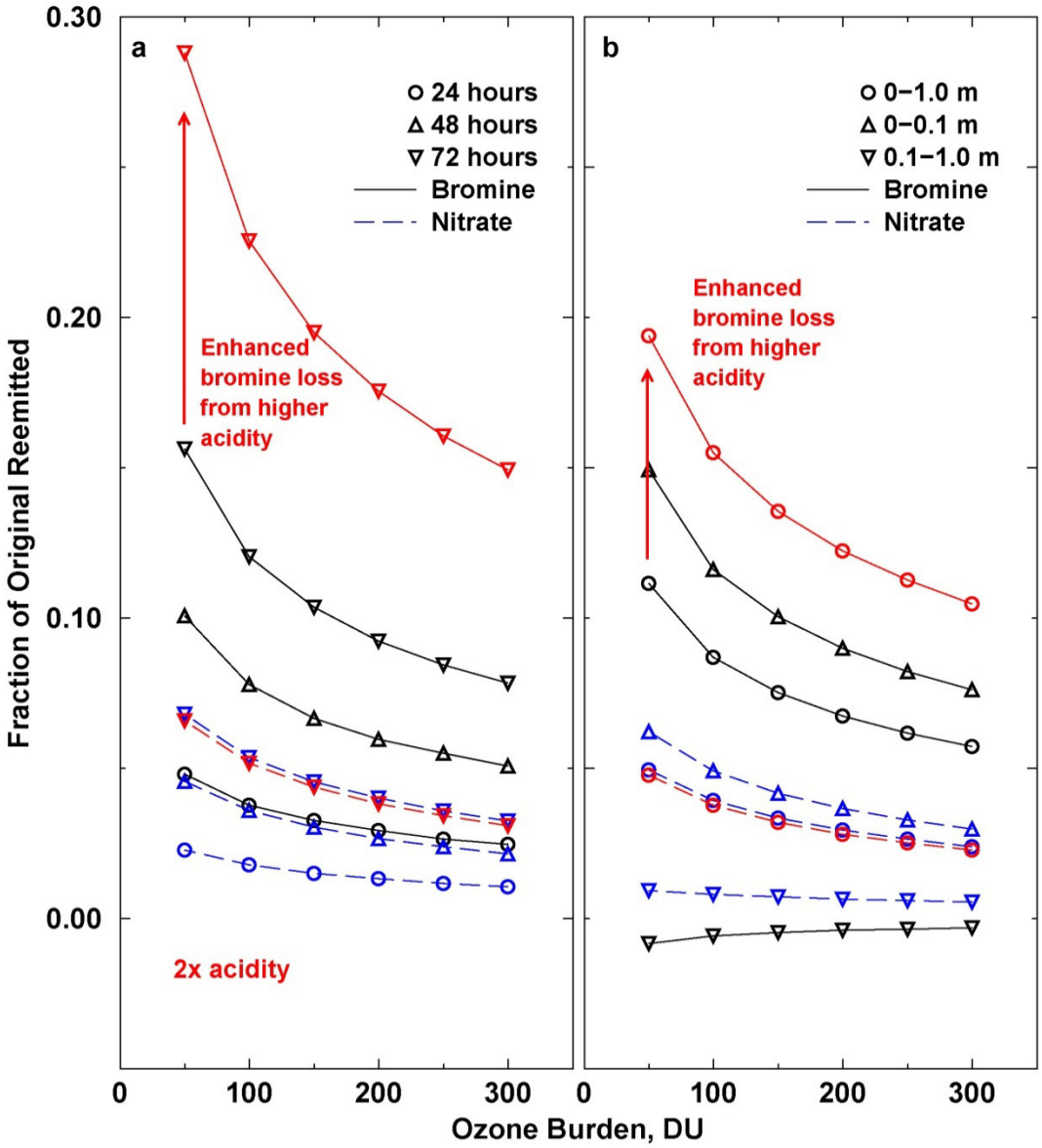

Fig. S5 MISTRA-SNOW (18) snowpack photochemistry model simulations of reversible deposition for bromine and nitrate in an idealized snowpack for different levels of total column ozone burden. (**a):** Simulations of bromine and nitrate emissions to the atmosphere from the surface-snow layer. (**b):** Simulations for the upper 1 m of the snowpack. Although nitrate re-emission from the surface snow and snowpack increases with decreased ozone burden, increases are much larger for bromine. Moreover, increased acidity (shown in red) has little or no impact on the re-emission rate of nitrate but substantial impact on bromine since associated reactions are acid catalyzed.

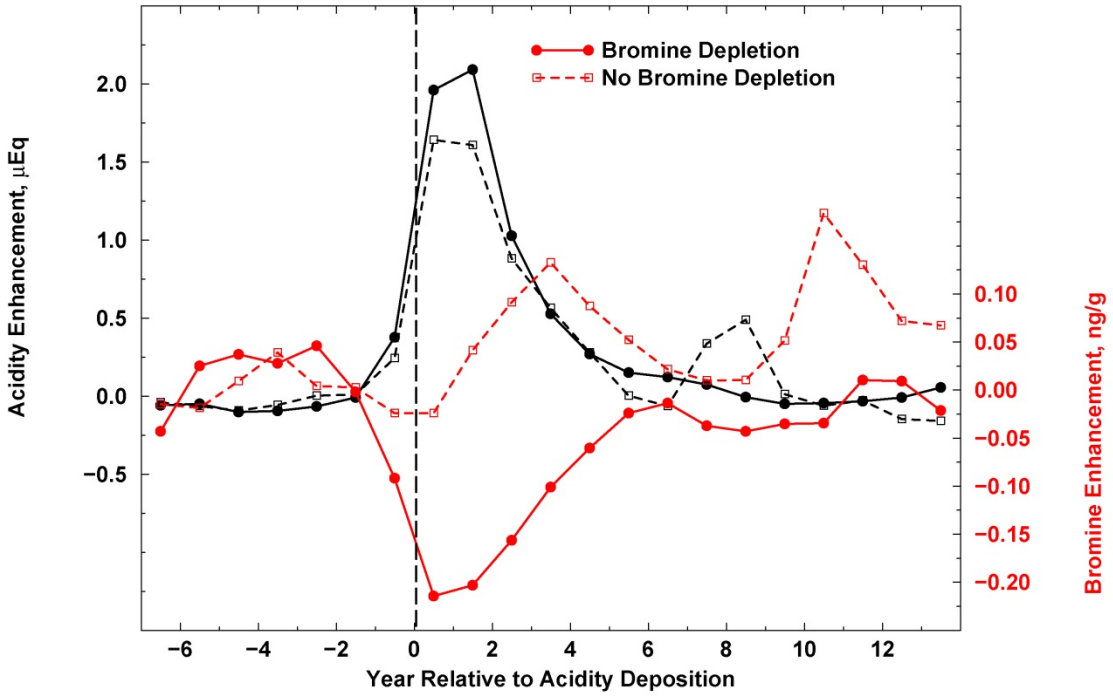

Fig. S6 Superposed epoch analysis for the 100 high acidity events between 10ka and 25ka in the WD ice core. All fallout events with annual average acidity concentrations >3.0 µeq L^{-1} (µEq) were included except those during the 17.7ka Mt. Takahe event. Shown are stacked acidity and bromine concentration enhancements, with enhancement defined as the annual concentration minus the average during the seven years preceding the start of enhanced acid deposition. Of the 100 events, 30 showed no bromine depletion on average during the four years following the start of enhanced acid deposition and corresponding to the period of highest acidity. Even though acid concentrations were similar for events with and without bromine depletion, the lack of bromine depletion for 30% of the events clearly demonstrates that high snow acidity alone is not sufficient to cause bromine depletion. Results also suggest that about 70% of large volcanic eruptions during this period were associated with stratospheric ozone loss that led to enhanced surface UV and loss of bromine from the snow, consistent with studies showing that many, but not all, modern eruptions result in measureable stratospheric ozone depletion (1, 2).

`

Comparisons to Modern Ozone Depletion

The seasonality and duration of increased surface UV from modern ozone depletion and the postulated 17.7ka ozone depletion may have been different. Modern chlorofluorocarbon-driven ozone loss and increased surface UV largely are springtime phenomena since increased UV persists only from sunrise until the Antarctic stratosphere isolated by the strong winter polar vortex mixes with mid- and low-latitude air as the vortex breaks down. For the postulated 17.7ka ozone hole, however, the source volcano was at 76^{o}S and presumably erupting throughout the year. While stratospheric halogen and sulfur concentrations may have been somewhat reduced by a weakened summertime vortex, the paleo-ozone hole likely persisted throughout the austral summer, leading to much greater integrated UV exposure each year and thus greater bromine loss.

Demonstrating enhanced bromine loss in near-surface snow in response to the modern anthropogenic ozone depletion requires a suitable ice core record. First, it is clear from modern observations (e.g., SI Appendix, Fig. S4) and snowpack photochemical modeling that bromine is reversibly deposited in polar snow. Most of the originally deposited bromine will be re-emitted to the atmosphere at low accumulation sites even under normal UV illumination, while bromine concentrations preserved in snow at high accumulation sites will be relatively insensitive to enhanced UV because the snow will be buried and cut off from UV and ventilation too quickly for significant UV-enhanced re-emission to occur. The ideal accumulation rate seems to be 100 kg/m^2/y based on the WD record. Second, because of the strong dependence of preserved bromine concentration on snow accumulation, any ice core record useful for assessing the impact of modern ozone depletion must show constant snow accumulation for at least the past 200 years to avoid accumulation-driven concentration changes and provide a robust record of background bromine prior to and during stratospheric ozone loss. Third, snowpack modeling (SI Appendix, Fig. S5) shows that UV-driven bromine re-emission is enhanced at higher acidities, and no evidence for increased acidity in Antarctica has been found during this period. Fourth, sea ice variability may alter bromine emissions and deposition to snow nearby, so suitable cores must be located well away from shorelines. To our knowledge, no Antarctic ice core records of bromine that match these criteria exist.

`

Atmosphere Ocean General Circulation Model Simulations

Observations and modeling indicate that the modern anthropogenic ozone hole has altered hydroclimate throughout the SH – including changes in atmospheric (34) and therefore oceanic circulation (34, 35), surface temperature (34), and precipitation (36-38). Specifically for precipitation, prescribed ozone depletion in model simulations resulted in a southward shift in Hadley circulation and the extra-tropical westerly jet (36), leading to subtropical moistening and mid-latitude drying similar to recent observations (Fig. 5). Increasing greenhouse gas concentrations are thought to have a broadly similar impact on SH climate, confounding the attribution of recent climate changes (39).

To evaluate the potential climate impact of a springtime ozone hole ~17.7k years ago, we used the COSMOS coupled Atmosphere Ocean General Circulation Model (AOGCM) initialized to Last Glacial Maximum (LGM) environmental conditions (40). The atmosphere model component ECHAM5 (41) was used at T31 resolution (~3.75°) with 19 vertical levels. The ocean component was MPIOM (42) with a curvilinear Arakawa-C grid and a formal horizontal resolution of ~1.8º x 3º. Forty unevenly spaced layers represented the vertical domain. For the ozone hole simulation, ozone concentrations from September through December each year were modified from standard levels (>1 ppmv) to 0.1 ppmv in height layers above 50 hPa over the latitude range 60^{o}S to 90^{o}S, since similar patterns of springtime ozone depletion have been observed during the modern ozone hole (43). This simulation with ozone depletion extended for 200 years.

Comparisons between 100-year averages of net precipitation (precipitation minus evaporation or P-E), 10 m wind velocity, and surface air temperature with the initial LGM climate and during the last 100 years of the 200-year ozone-hole simulation indicate that springtime ozone depletion could have had significant impacts on SH climate. Simulated changes in zonally averaged net precipitation (SI Appendix, Fig. S7) are similar both in latitudinal pattern and magnitude to those ascribed to modern stratospheric ozone depletion. Specifically, the model simulates drier conditions from ~6^{o} to ~22^{o}S and from ~41^{o} to ~58^{o}S, with moistening from ~22^{o} to ~41^{o}S and south of ~58^{o}S. As with the modern ozone hole (44), westerly winds in the region of the Drake Passage increase, with zonally averaged winds at 60^{o}S increasing 5% to 10% particularly during austral summer (DFJ) (SI Appendix, Fig. S7). The magnitude of the wind increase at 60^{o}S, however, is lower in the LGM simulation.

Temperatures also change in the 60^{o}S region particularly in the Pacific and Atlantic sectors, with simulated long-term (>100 year), quasi-equilibrium increases in annual LGM surface temperatures of 0.4^{o} to 0.8^{o} C as a result of ozone depletion (SI Appendix, Fig. S7). These increases are in agreement with modern quasi-equilibrium warming simulated using a coarse (1^{o}) model resolution (45), although similar experiments using a finer (0.1^{o}) model resolution simulated cooling over Antarctica but warming over the Southern Ocean (45). Additional published model simulations suggest a two-stage response to modern ozone depletion (46) – initial transient cooling followed by slower (decadal-scale) warming. The quasi-equilibrium

`

LGM responses reported here should not be confused with transient responses simulated for modern stratospheric ozone depletion (47).

The AOGCM-simulated changes in climate driven by persistent ozone depletion during the LGM also provide a possible means to change ventilation of the deep ocean around Antarctica exactly at the time hypothesized by Schmitt et al. (48) (Figs. 1, 2) to explain large changes in atmospheric CO_2 and stable carbon isotopes of CO_2 and increased upwelling. These include increases in the westerly wind belt around Antarctica and warming, particularly in the Pacific and Atlantic sectors of coastal Antarctica.

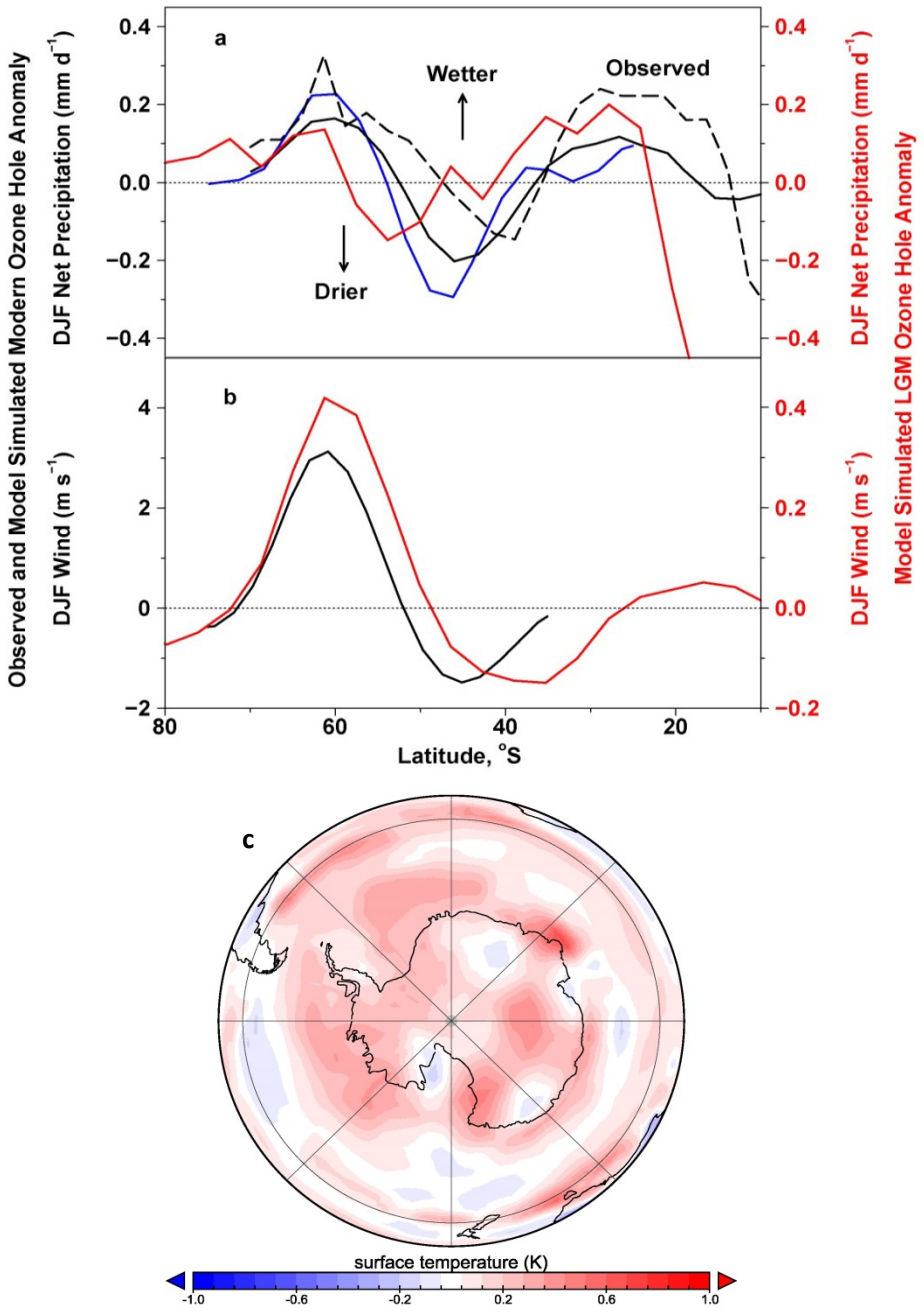

Fig. S7 Observed and model-simulated austral summer anomalies in hydroclimate associated with modern and postulated 17.7ka stratospheric ozone depletion. (a): Observed (black dashed (36) and modeled (modern: blue (38) and black (36) solid, LGM: red) zonal average changes in austral summer precipitation**. (b):** Modeled (modern: black (38); LGM: red) zonal average changes in wind. **(c):** Simulated austral summer average surface temperature anomalies resulting from the 17.7ka ozone hole. Simulated hydroclimatic responses to stratospheric ozone depletion under LGM conditions qualitatively are similar to observations and modeling of the modern ozone hole, but changes in winds are muted.

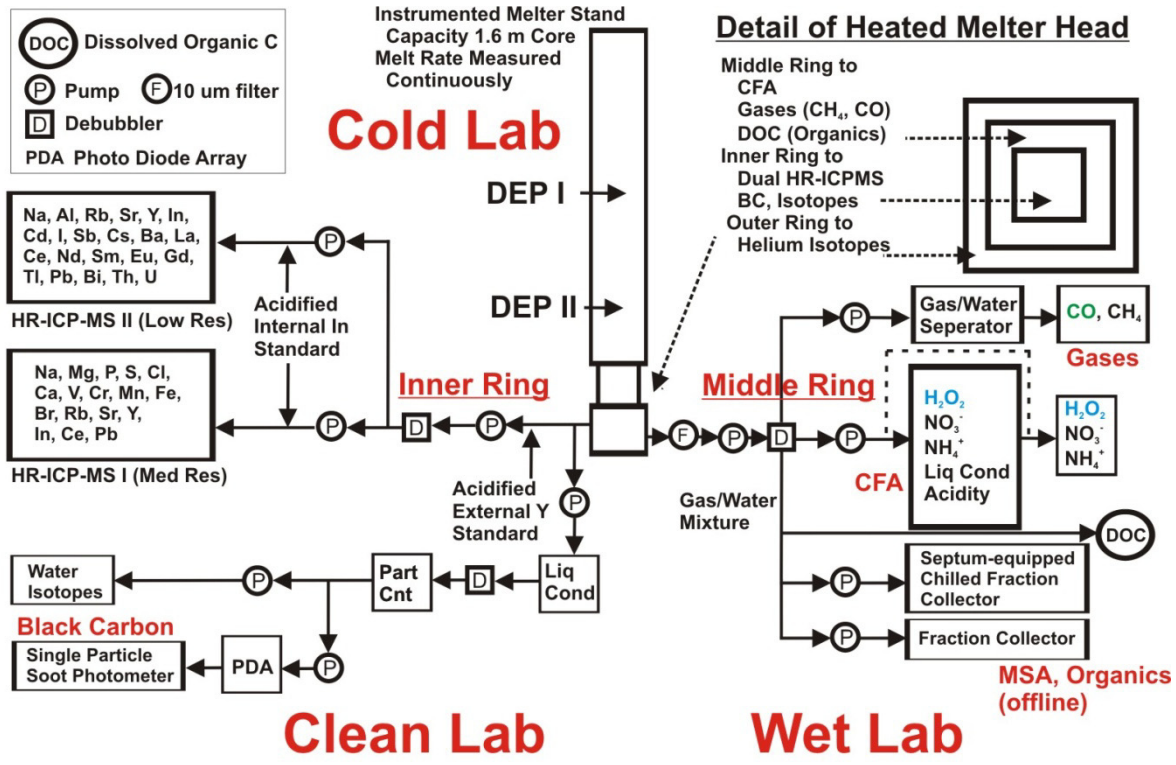

Fig. S8 Schematic of the CFA-TE-BC-GAS analytical system used for high-resolution, continuous analyses of WD, Byrd, and other ice cores. For replicate analysis of the 17.7ka event in the WD core, 10 µm filters were added to the lines coming from the middle ring to capture tephra for single-particle microprobe analyses. Discrete samples were collected during the continuous analyses for subsequent measurements of helium isotopes and chemical species such as fluoride and bromide. Hydrogen peroxide (H_2O_2) was not measured below 2171 m.

`

SI Appendix References

1. Kutterolf S*, et al.* (2013) Combined bromine and chlorine release from large explosive volcanic eruptions: A threat to stratospheric ozone? *Geology* 41(6):707-710.
2. Solomon S*, et al.* (2016) Emergence of healing in the Antarctic ozone layer. *Science* 353(6296):269-274.
3. Banta JR, McConnell JR, Frey MM, Bales RC, & Taylor K (2008) Spatial and temporal variability in snow accumulation at the West Antarctic Ice Sheet Divide over recent centuries. *J. Geophys. Res.-Atmos.* 113(D23).
4. Hammer CU, Clausen HB, & Langway CC (1997) 50,000 years of recorded global volcanism. *Climatic Change* 35(1):1-15.
5. Baggenstos D (2015) Taylor Glacier as an archive of ancient ice for large-volume samples: Chronology, gases, dust, and climate. Ph.D. (University of California, San Diego).
6. McConnell JR (2002) Continuous ice-core chemical analyses using inductively Coupled Plasma Mass Spectrometry. *Environmental Science & Technology* 36(1):7-11.
7. McConnell JR*, et al.* (2014) Antarctic-wide array of high-resolution ice core records reveals pervasive lead pollution began in 1889 and persists today. *Scientific Reports* 4(5848):1-5.
8. McConnell JR & Edwards R (2008) Coal burning leaves toxic heavy metal legacy in the Arctic. *Proceedings of the National Academy of Sciences of the United States of America* 105(34):12140-12144.
9. Sigl M*, et al.* (2016) The WAIS Divide deep ice core WD2014 chronology - Part 2: Annual-layer counting (0-31 ka BP). *Clim. Past* 12:769-786.
10. McConnell JR*, et al.* (2007) 20th-century industrial black carbon emissions altered arctic climate forcing. *Science* 317(5843):1381-1384.
11. McConnell JR, Aristarain AJ, Banta JR, Edwards PR, & Simoes JC (2007) 20th-century doubling in dust archived in an Antarctic Peninsula ice core parallels climate change and desertification in South America. *Proceedings of the National Academy of Sciences of the United States of America* 104(14):5743-5748.
12. Sigl M*, et al.* (2015) Timing and climate forcing of volcanic eruptions for the past 2,500 years. *Nature* 523(7562):543-549.
13. Pasteris DR, McConnell JR, & Edwards R (2012) High-resolution, continuous method for measurement of acidity in ice cores. *Environmental Science & Technology* 46(3):1659-1666.
14. Rhodes RH*, et al.* (2015) Enhanced tropical methane production in response to iceberg discharge in the North Atlantic. *Science* 348(6238):1016-1019.
15. Rhodes R, Baker J, Millet M, & Bertler N (2011) Experimental investigation of the effects of mineral dust on the reproducibility and accuracy of ice core trace element analyses. *Chemical Geology* 286(3-4):207-221.
16. Maselli OJ*, et al.* (2017) Sea ice and pollution-modulated changes in Greenland ice core methanesulfonate and bromine. *Climate of the Past* 13:39-59.
17. Paris G, Sessions AL, Subhas AV, & Adkins JF (2013) MC-ICP-MS measurement of delta S-34 and Delta S-33 in small amounts of dissolved sulfate. *Chemical Geology* 345:50-61.

`

18. Thomas JL*, et al.* (2011) Modeling chemistry in and above snow at Summit, Greenland - Part 1: Model description and results. *Atmospheric Chemistry and Physics* 11(10):4899-4914.
19. Dibb JE, Ziemba LD, Luxford J, & Beckman P (2010) Bromide and other ions in the snow, firn air, and atmospheric boundary layer at Summit during GSHOX. *Atmospheric Chemistry and Physics* 10(20):9931-9942.
20. France JL*, et al.* (2011) Snow optical properties at Dome C (Concordia), Antarctica; implications for snow emissions and snow chemistry of reactive nitrogen. *Atmospheric Chemistry and Physics* 11(18):9787-9801.
21. Dunbar NW, Zielinski GA, & Voisins DT (2003) Tephra layers in the Siple Dome and Taylor Dome ice cores, Antarctica: Sources and correlations. *Journal of Geophysical Research-Solid Earth* 108(B8):11.
22. Dunbar NW, McIntosh WC, & Esser RP (2008) Physical setting and tephrochronology of the summit caldera ice record at Mount Moulton, West Antarctica. *Geological Society of America Bulletin* 120(7-8).
23. Palais JM, Kyle PR, McIntosh WC, & Seward D (1988) Magmatic and phreatomagmatic volcanic activity at Mt Takahe, West Antarctica,based on tephra layers in the Byrd ice core and field observations at Mt Takahe. *Journal of Volcanology and Geothermal Research* 35(4).
24. McIntosh WC, LeMasurier WE, Ellerman PJ, & Dunbar NW (1985) A reinterpretation of glaciovolcanic interaction at Mount Takahe and Mount Murphy, Marie Byrd Land, Antarctica. *Antarctic Journal of the United States* 19:57-59.
25. Francis P, Burton MR, & Oppenheimer C (1998) Remote measurements of volcanic gas compositions by solar occultation spectroscopy. *Nature* 396(6711):567-570.
26. Wilch TI, McIntosh WC, & Dunbar NW (1999) Late Quaternary volcanic activity in Marie Byrd Land: Potential Ar-40/Ar-39-dated time horizons in West Antarctic ice and marine cores. *Geological Society of America Bulletin* 111(10).
27. Wilch TJ (1997) Volcanic record of the West Antarctic ice sheet in Marie Byrd Land. (New Mexico Institute of Mining and Technology, Socorro).
28. Zredagostynska G, Kyle PR, & Finnegan DL (1993) Chlorine, fluorine, and sulfur emissions from Mount Erebus, Antarctica and estimated contribution to the Antarctic atmosphere. *Geophysical Research Letters* 20(18):1959-1962.
29. Cadoux A, Scaillet B, Bekki S, Oppenheimer C, & Druitt T (2015) Stratospheric ozone destruction by the Bronze-Age Minoan eruption (Santorini Volcano, Greece). *Scientific Reports* 5.
30. Anderson RF*, et al.* (2009) Wind-driven upwelling in the Southern Ocean and the deglacial rise in atmospheric CO^2. *Science* 323(5920).
31. Abbatt JPD*, et al.* (2012) Halogen activation via interactions with environmental ice and snow in the polar lower troposphere and other regions. *Atmos. Chem. Phys.* 12(14):6237-6271.
32. Mozurkewich M (1995) Mechanisms for the release of halogens from sea-salt particles by free-radical reactions. *Journal of Geophysical Research-Atmospheres* 100(D7):14199-14207.
33. Traversi R*, et al.* (2009) Study of Dome C site (East Antartica) variability by comparing chemical stratigraphies. *Microchemical Journal* 92(1):7-14.

`

34. Thompson DWJ*, et al.* (2011) Signatures of the Antarctic ozone hole in Southern Hemisphere surface climate change. *Nature Geoscience* 4(11):741-749.
35. Waugh DW, Primeau F, DeVries T, & Holzer M (2013) Recent changes in the ventilation of the southern oceans. *Science* 339(6119):568-570.
36. Kang SM, Polvani LM, Fyfe JC, & Sigmond M (2011) Impact of polar ozone depletion on subtropical precipitation. *Science* 332(6032):951-954.
37. Gonzalez PM, Polvani L, Seager R, & Correa GP (2013) Stratospheric ozone depletion: a key driver of recent precipitation trends in South Eastern South America. *Climate Dynamics*:1-18.
38. Polvani LM, Waugh DW, Correa GJP, & Son S-W (2011) Stratospheric ozone depletion: The main driver of twentieth-century atmospheric circulation changes in the Southern Hemisphere. *Journal of Climate* 24(3):795-812.
39. Son SW*, et al.* (2008) The impact of stratospheric ozone recovery on the Southern Hemisphere westerly jet. *Science* 320(5882):1486-1489.
40. Zhang X, Lohmann G, Knorr G, & Xu X (2013) Different ocean states and transient characteristics in Last Glacial Maximum simulations and implications for deglaciation. *Climate of the Past* 9(5):2319-2333.
41. Roeckner E*, et al.* (2006) Sensitivity of simulated climate to horizontal and vertical resolution in the ECHAM5 atmosphere model. *Journal of Climate* 19(16):3771-3791.
42. Marsland SJ, Haak H, Jungclaus JH, Latif M, & Roske F (2003) The Max-Planck-Institute global ocean/sea ice model with orthogonal curvilinear coordinates. *Ocean Modelling* 5(2):91-127.
43. WMO (2011) Global Ozone Research and Monitoring Project—Report No. 52. in *Scientific Assessment of Ozone Depletion: 2010*.
44. Thompson DWJ & Solomon S (2002) Interpretation of recent Southern Hemisphere climate change. *Science* 296(5569).
45. Bitz CM & Polvani LM (2012) Antarctic climate response to stratospheric ozone depletion in a fine resolution ocean climate model. *Geophysical Research Letters* 39.
46. Ferreira D, Marshall J, Bitz C, Solomon S, & Plumb A (2015) Antarctic Ocean and sea ice response to ozone depletion: A two-time-scale problem. *Journal of Climate* 28(3):1206-1226.
47. Solomon A, Polvani L, Smith K, & Abernathey R (2015) The impact of ozone depleting substances on the circulation, temperature, and salinity of the Southern Ocean: An attribution study with CESM1(WACCM). *Geophysical Research Letters* 42(13):5547-5555.
48. Schmitt J*, et al.* (2012) Carbon isotope constraints on the deglacial CO^2 rise from ice cores. *Science* 336(6082).